Walter, M. J., Thomson, A. R., Wang, W., Lord, O. T., Ross, J. A., McMahon, S. C., Baron, M. A., Melekhova, E., Kleppe, A. K., & Kohn, S. C. (2015). The stability of hydrous silicates in Earth's lower mantle: Experimental constraints from the systems MgO-SiO_2-H_2O and MgO-Al_2O_3-SiO_2-H_2O. *Chemical Geology*, *418*, 16-29. https://doi.org/10.1016/j.chemgeo.2015.05.001

Chemical Geology 418 (2015) 16–29

Contents lists available at ScienceDirect

Chemical Geology

journal homepage: www.elsevier.com/locate/chemgeo

The stability of hydrous silicates in Earth's lower mantle: Experimental constraints from the systems $MgO–SiO_2–H_2O$ and $MgO–Al_2O_3–SiO_2–H_2O$

M.J. Walter [a,*], A.R. Thomson [a], W. Wang [a,b], O.T. Lord [a], J. Ross [a], S.C. McMahon [a], M.A. Baron [a], E. Melekhova [a], A.K. Kleppe [c], S.C. Kohn [a]

[a] School of Earth Sciences, University of Bristol, Queen's Road, Bristol BS8 1RJ, United Kingdom
[b] Department of Earth Sciences, University College London, Gower Street, London WC1E 6BT, United Kingdom
[c] DIAMOND Light Source Ltd, Chilton, Didcot OX11 0QX, Oxfordshire, United Kingdom

ARTICLE INFO

Article history:
Accepted 1 May 2015
Available online 10 May 2015

Editor: K. Mezger

Keywords:
Phase D
Phase H
Hydrogen
Lower mantle
Hydrous silicate melt

ABSTRACT

We performed laser-heated diamond anvil cell experiments on bulk compositions in the systems $MgO–SiO_2–H_2O$ (MSH) and $MgO–Al_2O_3–SiO_2–H_2O$ (MASH) that constrain the stability of hydrous phases in Earth's lower mantle. Phase identification by synchrotron powder diffraction reveals a consistent set of stability relations for the high-pressure, dense hydrous silicate phases D and H. In the MSH system phase D is stable to ~50 GPa, independent of temperature from ~1300 to 1700 K. Phase H becomes stable between 35 and 40 GPa, and the phase H out reaction occurs at ~55 GPa at 1600 K with a negative dT/dP slope of ~− 75 K/GPa. Between ~30 and 50 GPa dehydration melting occurs at ~1800 K with a flat dT/dP slope. A cusp along the solidus at ~50 GPa corresponds with the intersection of the subsolidus phase H out reaction, and the dT/dP melting slope steepens to ~15 K/GPa up to ~85 GPa.

In the MASH system phase H is stable in experiments between ~45 and 115 GPa in all bulk compositions studied, and we expect aluminous phase H to be stable throughout the lower mantle depth range beneath ~1200 km in both peridotitic and basaltic lithologies. In the subsolidus, aluminous phase D is stable to ~55 GPa, whereas at higher pressures aluminous phase H is the stable hydrous phase. The presence of hydrogen may sharpen the bridgmanite to post-perovskite transition. The ambient unit cell volume of bridgmanite increases systematically with pressure above ~55 GPa, possibly representing an increase in alumina content, and potentially hydrogen content, with depth. Bridgmanite in equilibrium with phases D and H has a relatively low alumina content, and alumina partitions preferentially into the hydrous phases. The melting curves of MASH compositions are shallower than in the MSH system, with dT/dP of ~6 K/GPa. Phase D and H solid solutions are stable in cold, hydrated subducting slabs and can deliver water to the deepest lower mantle. However, hydrated lithologies in the lower mantle are likely to be partially molten at all depths along an ambient mantle geotherm.

1. Introduction

The lower mantle is the most massive potential hydrogen-bearing reservoir in Earth. There are several mechanisms whereby hydrous components may have been delivered to the deep mantle over geologic time, creating a long-lived hydrogen reservoir. As the planet accreted and grew in size, primordial volatiles may have become isolated in the deepest parts of the mantle. Primordial hydrogen could have been retained in a primitive lower mantle reservoir along with other volatile elements, and such a reservoir is supported by the isotopic composition of noble gases from mantle-derived samples (Marty, 2012; Mukhopadhyay, 2012; Halliday, 2013). Modest solubility of hydrous species in a global magma ocean may have allowed the mantle to retain significant hydrogen, especially if outgassing were inefficient, or if a relatively small fraction of late incoming metal in a giant impact equilibrated with the magma ocean (Mookherjee et al., 2008; Mysen et al., 2009; Hirschmann et al., 2012). The possibility that magma ocean crystallization occurred from the mid-lower mantle outward may have resulted in a deep basal magma body (Stixrude and Karki, 2005; Labrosse et al., 2007; Mosenfelder et al., 2007), which would be expected to concentrate incompatible elements like hydrogen. It is also possible that mantle overturn after crystallization delivered an unknown quantity of water and other volatiles into the deep mantle (Elkins-Tanton, 2008). And perhaps most importantly, billions of years of plate tectonics will have recycled lithosphere into the deep mantle with the potential to deliver hydrous components (Ohtani et al., 2001b; Komabayashi et al., 2004; Ohtani, 2005; Ohira et al., 2014). Indeed, melting at the top of the lower mantle, possibly related to subduction of hydrous components, has recently been suggested on the basis of a combination of experimental and seismic observations (Schmandt et al., 2014).

* Corresponding author. Tel.: +44 117 331 5007.
E-mail address: m.j.walter@bristol.ac.uk (M.J. Walter).

http://dx.doi.org/10.1016/j.chemgeo.2015.05.001

There are limited phase equilibrium data at the extreme P–T conditions of the lower mantle in volatile bearing systems. The amount of water that can be stored in silicate bridgmanite may be small, although the issue is not entirely resolved, with estimated solubility ranging over several orders of magnitude (Meade et al., 1994; Bolfan-Casanova et al., 2000; Murakami et al., 2002; Litasov et al., 2003; Bolfan-Casanova, 2005). If the water content of nominally anhydrous lower mantle phases is very low, then water might be stored in solid hydrous silicate phases, molten hydrous silicate, or possibly even as water–ice (Bina and Navrotsky, 2000; Schwager et al., 2004). Fundamental to modeling the behavior of hydrogen in the deep Earth is knowledge of the phase relations of the solids and liquids that can potentially host hydrogen at the extreme conditions of the lower mantle.

There is a rich diversity of dense hydrous silicates that are stable in mafic and ultramafic assemblages at upper mantle pressures and low to moderate temperatures (Ohtani et al., 2000; Ohtani et al., 2001b; Komabayashi et al., 2004; Ohtani et al., 2004; Ohtani, 2005). Water transport from the transition zone into the lower mantle is controlled primarily by the stability of phase D, an orthorhombic mineral with the ideal formula $MgSi_2H_2O_6$, which according to available data has a stability limited to about 45 GPa and, depending especially on its alumina content, possibly to temperatures exceeding 2000 K (Shieh et al., 1998; Shinmei et al., 2008; Ghosh and Schmidt, 2014; Pamato et al., 2015). It is also known that a high-pressure form of diaspore (α-AlOOH), called δ-AlOOH and with an orthorhombic symmetry very close to that of stishovite in the $CaCl_2$-type structure, is stable throughout the mantle depth range and may be present in suitably aluminous and hydrated lithologies (Suzuki et al., 2000; Ohtani et al., 2001a; Tsuchiya et al., 2002; Sano et al., 2008). Mg and Si can substitute into the δ-AlOOH structure, causing subtle symmetry changes probably related to disorder of hydrogen (Suzuki et al., 2000; Komatsu et al., 2011).

Recently, the discovery of a new phase closely related to δ-AlOOH, with the stoichiometric composition $MgSiH_2O_4$, was predicted by ab initio methods with a calculated stability limit of ~50 GPa (Tsuchiya, 2013), potentially extending the depth range to which hydrous magnesian silicates can deliver water into the lower mantle. This new phase has now been observed in experiments up to 50 GPa in the $MgO–SiO_2–H_2O$ (MSH) system, although an upper pressure limit has yet to be determined, and has been given the name phase H (Nishi et al., 2014). The structure of phase H has recently been shown to have orthorhombic *pnnm* symmetry (Bindi et al., 2014; Nishi et al., 2014). Given the similarity in crystal structures, and because it has already been shown that Mg and Si dissolve into δ-AlOOH, it may be that a considerable or complete solid solution exists between these phases, and that an (Mg,Si,Al)OOH phase may be stable throughout much or all of the mantle depth range in common mantle lithologies. Indeed, aluminous phase H has been found to be stable to the base of the mantle in a composition with ~30 mol% Al_2O_3 in the system $MgO–Al_2O_3–SiO_2–H_2O$ (MASH) (Ohira et al., 2014).

Here we investigate phase relations in the systems $MgO–Al_2O_3–H_2O$ (MSH) and $MgO–Al_2O_3–SiO_2–H_2O$ (MASH) at lower mantle pressures and high temperatures using the laser-heated diamond anvil cell, with the aim of determining the stability of hydrous phases and constraining melting temperatures of model hydrated mantle lithologies. Synchrotron-based powder diffraction is used to identify phases in run products, constraining the stability of phases D and H in model peridotitic and basaltic lithologies in these systems. We use thermal signal processing and high-resolution imaging to constrain melting temperatures, and evaluate the stability of solid and liquid hydrous phases in these systems at lower mantle conditions.

2. Experimental and analytical methods

2.1. Starting compositions

The compositions of the seven starting mixtures used in this study, two in the MSH system and five in the MASH system, are provided in Table 1 and are shown on Fig. 1. In each system we investigate both MgO-rich and SiO_2-rich compositions in order to explore differences between model peridotitic and basaltic systems, respectively. In the MSH system, compositions have ~9 to 13 mol% H_2O, while in the MASH system compositions have ~4 to 7 mol% H_2O. Al_2O_3 contents in the MASH system range from ~2 to 10 mol%, again to emulate differences between peridotitic and basaltic bulk compositions.

Table 1
Experimental starting compositions (mol fraction).

Composition	MgO	Al_2O_3	SiO_2	H_2O
MSH1	0.500	–	0.372	0.128
MSH2	0.320	–	0.590	0.090
MASH1	0.487	0.025	0.450	0.038
MASH2	0.477	0.046	0.418	0.059
MASH3	0.443	0.022	0.497	0.038
MASH6	0.452	0.096	0.386	0.066
MASH7	0.405	0.085	0.445	0.065

Starting compositions are synthesized as mixtures of anhydrous silicate glass and brucite. In the MSH system, $MgSiO_3$ glass was synthesized by fusing an ~1 g stoichiometric mixture of reagent grade MgO and SiO_2 powders in a Pt capsule inserted into a 1 atm furnace at ~1680 °C. Crystal-free glass forms upon quenching into water. Glass mixtures in the MAS system are the same as those used in previous work (Walter et al., 2004), and were synthesized under similar conditions. Quenched glasses were ground and refused once, and then reground to a fine powder under alcohol. Glass powders were mixed with natural brucite ($Mg(OH)_2$), the phase purity of which was confirmed by X-ray diffraction that showed only brucite reflections and no indication of carbonate that can form by reaction with air (Ghosh and Schmidt, 2014). Mixtures were ground typically for 2 h in an agate mortar. Pt black was added (10% by weight), and samples reground under acetone until the average Pt grain size was ~1 μm or less.

2.2. Diamond anvil cell experiments

2.2.1. High pressure

Experiments were made in 'Princeton-type' symmetric diamond anvil cells, incorporating Type Ia diamonds with culet diameters ranging from 120 to 250 μm. Samples are held in Re gaskets pre-indented to a thickness of ~50 μm. Chambers ~ 30 μm in diameter are laser-drilled in the indentation. The chamber size is purposefully designed in order to match the laser focal size in order to heat as much of the sample as uniformly as possible, so as to minimize the amount of un-reacted or partially reacted material that can complicate interpretation of diffraction measurements. An added benefit of a small chamber size is that multiple chambers can be used in experiments with culet sizes of 200 (3-holes) or 250 μm (4-holes), as shown in Fig. 2. This multiple chamber design allows a range of temperatures and pressures to be investigated in a single run. Samples are loaded as powders directly into the sample chambers. We chose not to use a thermally insulating pressure medium in this study in order to avoid the possibility of sample contamination, partial reactivity with insulating material, or H_2O loss from the heated sample environment.

Pressure is measured using the Raman shift of the singlet peak of the diamond anvil at the culet surface that is related to stress in the (001) direction (Hanfland et al., 1986). In this way we avoid putting ruby (Al_2O_3) grains in the sample chamber for a pressure marker, and unlike ruby, the signal from this peak remains strong and highly resolvable even to the Mbar range. Raman measurements are made with a Jobin-Yvon T64000 Raman spectrometer in either single- or triple-additive mode and using a confocal aperture of 200 μm. Previous workers have used the high frequency edge of the entire Raman signal to construct a pressure scale (Akahama and Kawamura, 2010). However, we find that the singlet peak is a robust feature in most cases when making highly confocal measurements that can be precisely fitted, typically

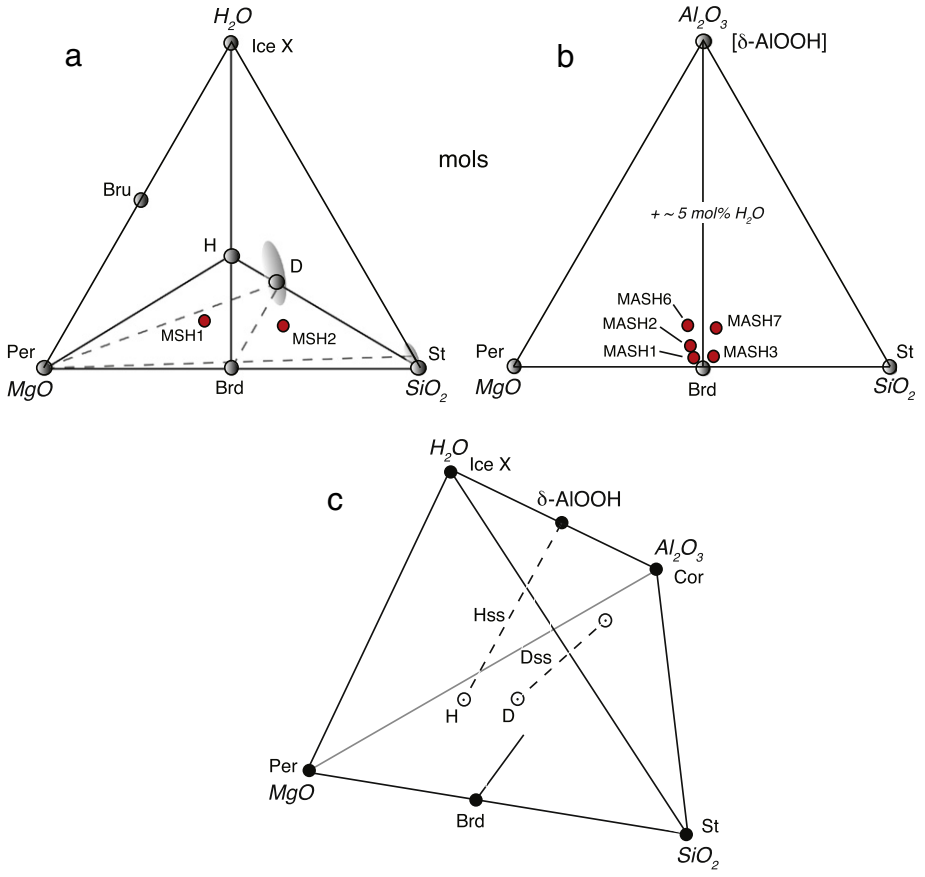

Fig. 1. Starting compositions in the (a) MSH and (b) MASH systems used in this study. Compositions in the MASH system are projected from H_2O. Figure (c) shows the MASH quaternary with the compositions of hydrous and anhydrous phases relevant to the deep mantle. Per = periclase; Brd = bridgmanite; St = stishovite; Bru = brucite; D = phase D; Dss = phase D solid solution; H = phase H; Hss = phase H solid solution; IceX = high pressure form of water ice. Shown on (a) are some possible relevant tie lines between phases in the MSH system.

with a resolution of better than 1 cm^{-1}. The Raman shift itself is calibrated relative to the ruby scale (Mao et al., 1986). We find that the calibration is sample material dependent, so the calibration was made with the same starting materials as used in this study. The Raman shift is calibrated against the R1 fluorescence shift of ruby, and a Raman shift versus pressure calibration curve constructed as shown in Fig. 2. The straight line fit to the data yields a slope of 0.501. The precision to which pressure can be measured with the Raman peak is about 0.1 GPa, although the accuracy is poorer, ~2 GPa due to uncertainty in measuring the ruby pressure. This potentially can be much improved via calibration using EoS measurements of internal standards. We measured the unit cell volume of Pt at high pressure in experiments at 116 and 123 GPa, and based on the EoS of Pt (Dorogokupets and Dewaele, 2007) there is good agreement with extrapolation of the ruby-based calibration curve (Fig. 3). Pressures are measured before and after heating. Typically post-heating pressures are within 5% of the pre-heating pressure. All reported pressures are post-heating measurements, and no correction has been made for thermal pressure during heating, which at the relatively modest temperatures of these experiments may be of the order 10% or less of the measured pressure (Heinz, 1990; Belonoshko and Dubrovinsky, 1997).

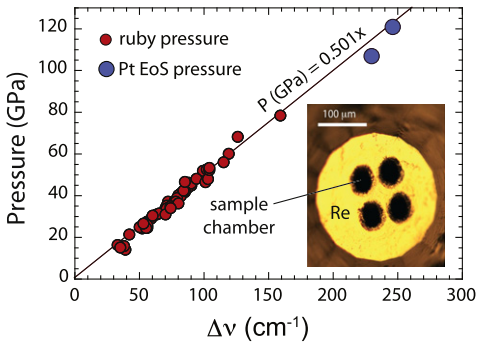

Fig. 2. Calibration of the Raman shift of the diamond singlet mode as measured at the culet surface. The singlet peak is related to stress along the (001) axis. The Raman shift is calibrated relative to the ruby scale, as shown by the red circles. The fitted curve, which is forced through the origin, yields a slope of 0.501. The large blue circles show in situ pressure measurements using the EoS of Pt, and are not included in the fit. The inset shows a Re gasket with four sample chambers filled with starting material.

2.2.2. High temperature

Laser heating in a double-sided geometry produces high-temperatures. The system at Bristol comprises two 100 W fiber lasers (1070 nm, SPI Red Laser) operating in a Gaussian output mode. The laser beams are modified by a combination of beam shaping lenses (pi-Shaper) and beam expanders to a flat-top profile of a size to match the dimensions of the sample chamber (~20–30 μm). In this way the energy density can be manipulated to minimize radial temperature gradients. Water-cooled Mitutoyo (10×) NIR long working distance apochromatic lenses are used to focus the lasers onto the sample. Two heating styles were used, 'isothermal' and 'ramped'. In isothermal experiments samples are heated to a target maximum temperature and held for between 5 and 120 min before quenching by shutting off the laser power. In ramped experiments laser power is continually incremented by 0.2 W on each side every 4 s until quenching. Ramped experiments are used to detect thermal perturbations that typically manifest as a temperature 'plateau', i.e., relatively constant temperature

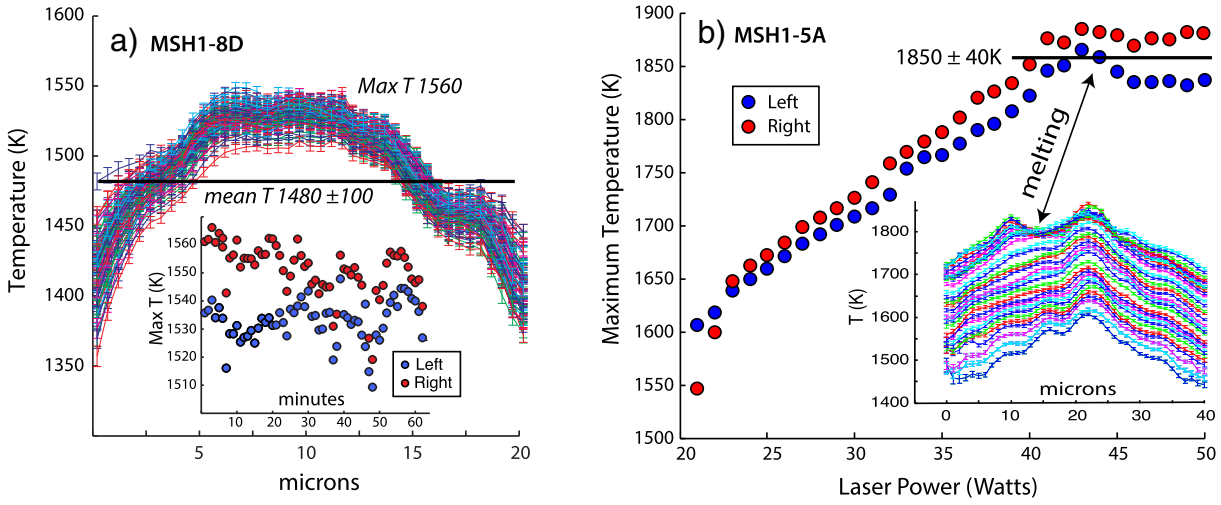

Fig. 3. (a) Radial temperature profile across the heated spot in a typical experiment. The chamber size in this case is ~20 μm. The maximum temperature in the sixty-minute experiment was 1560 K, and the mean temperature over this duration 1480 ± 100 K (2σ). Error bars reflect the precision of Wien fits and are ±1σ. The inset shows peak temperatures measured on both sides of the DAC as a function of experiment duration. (b) Example of a typical ramped experiment showing maximum temperatures measured on both sides of the DAC as a function of total laser power. There is a clear thermal perturbation that manifests as a temperature plateau. The plateau temperature is calculated as the mean of measured maximum temperatures on both sides from the onset of the plateau, and in this case is 1850 ± 40 K (2σ). The inset shows radial temperature profiles, and illustrates the change commonly observed in the profile at the plateau. We attribute the thermal perturbation to melting.

with increasing power. The interpretation of these perturbations is discussed below.

Temperature is measured using spectroradiometric techniques that have been described in detail elsewhere (Walter and Koga, 2004). In short, incandescent emission from the heated spot is focused (50× magnification) onto the vertical entrance slit of an imaging spectrometer. The slit has a width of 100 μm, which corresponds to an ~2 μm strip across the heated sample at the object plane. The system optical resolution has been measured to be ~2 μm, although the CCD-resolution provides temperatures calculated at ~0.5 μm intervals. The intensity of the thermal emission is normalized with a NIST-calibrated W-lamp of spectral radiance, and fitted with a Wien function over a wavelength range of 570–830 nm. Precision in measured temperatures based on the goodness of the linear fits is typically 2 to 4 K, indicating that chromatic dispersion is minimal in the optical system (Walter and Koga, 2004). The laser heating and temperature measurement systems are described in more detail in Lord et al. (2014).

Fig. 3a shows a typical example of an isothermal heating measurement in which a maximum temperature of 1560 K is achieved. However, the radial gradient indicates temperatures of ~1350 K at the edge of the sample, and this range of ~200 K (±100 K) is typical of the experiments reported here. Fig. 3a also illustrates our ability to maintain stable heating conditions for extended duration, with temperature variation at a given position on the sample of the order ±25 K. In Table 2 (MSH system) and Table 3 (MASH system) we report run conditions, and both maximum temperatures and mean temperatures are provided for all isothermal experiments. Mean temperature is calculated as the average of all temperatures measured across a 20–25 μm strip across the sample and throughout the duration of the experiment as shown in Fig. 3a, and uncertainty estimated as ±2σ of the mean. Here we will refer to mean temperatures when discussing experimental conditions, and all subsolidus data points are plotted on the basis of mean temperatures. Fig. 3b shows a typical temperature vs. laser power ramp, with an unambiguous thermal perturbation at ~1850 K. We determine the temperature on this heating plateau by averaging temperatures on both sides starting from a selected power at which we estimate the plateau to begin. We also note that typically there is a change in the radial temperature distribution (Fig. 3b inset) corresponding to the temperature plateau, often resulting in a central minimum surrounded by an annulus of higher temperature material. Movement apparent visually within the sample frequently accompanies the plateau and change in profile, particularly in the MSH system. As discussed below, we attribute these thermal perturbations to melting.

2.3. Synchrotron X-ray diffraction

Powder X-ray diffraction measurements were made on P–T quenched and high-P samples at beamline I15 of the Diamond Light Source, UK. Monochromatic X-rays with wavelengths of either 0.4133 or 0.4246 Å were focused to 65 × 65 μm and further collimated by a tungsten pinhole to give a 20 μm beam diameter. Diffracted X-rays were detected with a MAR345 image plate (MarResearch), with the sample to detector distance calibrated to within ±10 μm using a silicon standard. Diffraction patterns are reduced to 1D profiles using the FIT2D software (Hammersley et al., 1995). Profiles are analyzed using Macdiff software for phase identification. Full profile fitting for the calculation of unit cell volumes was performed using the Le Bail method (Lebail et al., 1988), as implemented in the GSAS suite of programs (Lazor et al., 1993; Toby, 2001).

3. Results

Table 2 (MSH) and Table 3 (MASH) list run conditions and phases identified by X-ray diffraction. In addition to the silicate and oxide phases, all patterns contain diffraction lines from the Pt black absorber as well as a variable contribution from the Re gasket. Interference from these lines does not preclude identification of phases since no peaks from these materials exist at d-spacing greater than 2.4 Å (1 atm), and all phases reported on here, with the exception of periclase, have major peaks at larger d-spacing. Some experiments contain traces

Notes to Table 2:
Mean T and 2s error as described in text; Ramp = ramped heating experiment.
Brd = bridgmanite; Per = periclase; St = stishovite; D = phase D; H = phase H; (Bru) = unreacted brucite in starting material.
Phases are listed according to estimated order of abundance based on the relative intensity of major diffraction peaks.
Brucite is interpreted as inherited from the starting material.

Table 2
Experimental conditions and results in the system MSH.

Experiment	Hole	P (GPa)	T max (K)	Mean T (K)	2σ	Time (min)	Phases
MSH1-1	A	39	1840	1700	100	6	D + St + Per + Brd
	B	35	1900	1770	120	6	D + St + Per + Brd
	C	30	1780	1700	100	6	D + St + Per
	D	36	1890	–	80	Ramp	D + St + Per
MSH1-3	A	47	1930	–	50	Ramp	Brd + H + St + Per + D
	B	46	2100	–	50	Ramp	Brd + St + Per
	C	49	1840	1750	100	6	Brd + St + Per
	D	50	1900	1800	100	5	Brd + St + Per
MSH1-4	B	27	1650	1550	100	7	D + Per + St
	C	41	1840	–	40	Ramp	St + D + Per
	D	30	1720	1615	100	7	St + D + Per
MSH1-5	A	33	1850	–	60	Ramp	D + Per + St + Brd
	B	32	1640	1590	80	15	D + St + Per
	C	30	1600	1490	100	30	D + Per + St
	D	30	1500	1400	100	60	D + St + Per + Brd
MSH1-6	B	46	1800	1660	100	17	Per + H + D + St + Brd
	C	41	1600	1525	120	22	H + Per + D + St + Brd
	D	40	1600	1450	100	30	H + Brd + Per + D + St
MSH1-7	A	40	1780	1635	100	20	D + St + Per + Brd (Bru)
	B	41	1720	1590	120	20	D + Brd + St + H + Per (Bru)
	C	41	1640	1505	80	60	D + H + St + Per + Brd (Bru)
	D	40	1490	1400	80	60	D + Per + Brd + St (Bru)
MSH1-8	B	33	1710	1610	90	20	D + Per + St (Bru)
	C	34	1480	1350	120	120	D + Per + St + Brd (Bru)
	D	35	1560	1480	100	60	D + Per + St + Brd (Bru)
MSH1-9	A	58	1880	1590	160	15	Brd + H + Per
	B	53	1660	1520	120	20	Brd + H + Per
	C	54	1620	1450	100	40	Brd + H + Per
	D	56	1450	1350	120	90	Brd + H + Per
MSH1-10	A	53	1865	–	60	Ramp	St + Brd + Per + H
	B	48	1720	1600	120	20	Brd + H + Per + St + D
	C	47	1550	1460	100	45	Brd + H + St + D + Per
	D	47	1500	1350	120	55	Brd + H + D + St
MSH1-11	A	65	1550	1450	100	20	Brd + Per
	B	66	1410	1350	100	30	Brd + Per
	C	56	1700	1575	100	10	Brd + Per + H
	D	57	1790	1650	140	6	Brd + Per
MSH1-12	B	64	1950	1810	100	7	Brd + Per
	C	71	2220	–	100	Ramp	Brd + Per
MSH2-1	A	40	1840	1715	100	5	D + St + Per + Brd
	B	34	1820	1720	100	4	D + St + Per + Brd
MSH2-2	B	39	1750	1650	100	15	D + St + H + Per + Brd
	C	44	1905	–	50	Ramp	Brd + St + D + H + Per
	D	40	1865	–	50	Ramp	D + St + H + Per + Brd
MSH2-3	A	39	1835	–	30	Ramp	Brd + H + St + D + Per
	B	36	1800	1710	50	5	D + St + Per
	C	45	1950	1730	130	5	D + St + H + Per + Brd
	D	43	1810	1690	100	7	Brd + St + H + Per
MSH2-4	B	30	1780	–	70	Ramp	St + Per + D
	D	59	1990	–	80	Ramp	Brd + St
MSH2-6	A	36	1825	–	35	Ramp	D + St + Per (Bru)
	B	40	1600	1505	80	15	St + H + D + Brd + Per
	C	40	1530	1440	80	30	H + St + D + Per + Brd
	D	36	1350	1300*	100	40	St + D + H + Per + Brd
MSH2-7	A	55	1885	–	50	Ramp	Brd + St
	B	55	1760	1660	80	12	Brd + St
	C	53	1620	1535	60	25	Brd + St + H
	D	55	1520	1450	60	60	Brd + St + H
MSH2-8	A	31	1760	1610	100	20	D + St + Per (Bru)
	B	32	1660	1520	80	50	D + St + Per (Bru)
	C	33	1460	1350	80	60	D + St + Per (Bru)
	D	29	1350	1300*	100	120	D + St + Per (Bru)
MSH2-9	A	44	1730	1630	100	20	H + St + D + Per + Brd (Bru)
	B	49	1700	1585	80	25	H + St + Brd + D + Per (Bru)
	C	48	1550	1450	100	60	H + Brd + St + D + Per (Bru)
	D	45	1400	1350	100	120	H + Brd + St + D + Per (Bru)
MSH2-10	A	70	1800	1600	140	14	Brd + St
	B	64	1570	1450	80	25	Brd + St + H
	C	65	1450	1350	100	90	Brd + St + H
	D	63	2090	–	50	Ramp	Brd + St
MSH2-11	A	78	2200	–	60	Ramp	Brd + St
	B	74	2175	–	100	Ramp	Brd + St
	C	73	1970	1875	80	10	Brd + St

Table 3
Experimental conditions and results in the system MASH.

Experiment	Hole	P (GPa)	Max T (K)	Mean T (K)	2σ	Time (m)	Phases
MASH1-1	A	68	1750	1670	70	10	Brd + H + Per
	B	69	2230	–	60	Ramp	Brd + H + Per
	C	70	2000	1850	100	7	Brd + H + Per
MASH1-2	A	56	1850	1620	150	12	Brd + H + St + Per + D
	C	53	1780	1605	75	12	Brd + H + Per + St + D
	D	54	2110	–	50	Ramp	Brd + D + St + Per
MASH1-3	A	96	1980	1780	90	10	Brd + H + Per
MASH1-4	A	114	1960	1740	60	12	Brd + H + Per
MASH1-5	A	46	1900	1760	120	20	D + Brd + Per
	B	47	1650	1550	90	30	D + Brd + Per + H
	C	50	2050	–	50	Ramp	Brd + St + H + Per
MASH1-6	B	34	1750	1670	60	15	D + Brd + Per + cor
	C	35	1510	1440	60	20	D + Brd + Per + cor
MASH1-7	A	42	1890	1750	100	15	D + Brd + Per
	B	40	1720	1580	120	20	D + Brd + Per
	C	40	1520	1460	60	20	D + Brd + Per
	D	37	2050	–	100	Ramp	–
MASH1-8	A	39	1900	–	60	Ramp	–
	B	37	1950	–	50	Ramp	–
	C	43	2000	–	100	Ramp	–
MASH1-9	A	93	2300	–	100	Ramp	–
MASH2-1	A	78	1720	1510	140	12	Brd + H + Per
	B	62	1900	1700	100	10	Brd + H + Per
MASH2-2	A	56	2120	–	60	Ramp	Brd + H + Per + St
	B	65	1580	1450	120	20	Brd + H + Per
	D	49	1850	1670	120	15	Brd + D + Per + St
MASH2-3	A	98	1830	1720	80	12	Brd + H + Per
MASH2-4	A	116	1890	1750	100	12	Brd + H + Per
MASH2-4*	A	116	1890	1750	100	12	Brd + PPv + H + Per
MASH2-5	B	47	2100	–	100	Ramp	–
MASH2-6	A	95	2350	–	100	Ramp	–
MASH3-1	A	72	2145	–	60	Ramp	Brd + H + St
	B	62	1920	1680	130	13	Brd + H + St
	C	73	1950	1710	150	13	Brd + H + St
MASH3-2	A	55	1850	1750	120	12	Brd + H + St + D
	B	52	2135	–	60	Ramp	Brd + H + St
	C	53	1530	1435	100	15	Brd + H + St + D
	D	49	1890	1755	120	10	Brd + H + St + D
MASH3-3	A	95	1960	1730	140	12	Brd + H
MASH6-1	A	77	1660	1525	140	13	Brd + H + Per
	B	66	1760	1550	140	13	Brd + H + Per
	C	74	2190	–	50	Ramp	Brd + H + Per
MASH6-2	A	50	1900	1740	120	10	Brd + H + Per + D + St
	B	60	2050	1825	180	7	Brd + H + Per
	C	56	2080	–	150	Ramp	Brd + H + Per + St
	D	51	1720	1515	130	20	Brd + D + H + Per
MASH7-1	A	81	1980	1760	140	10	Brd + H + St
	B	78	1550	1450	100	15	Brd + H + St
	C	73	2150	–	70	Ramp	Brd + H + St
MASH7-2	A	63	1670	1490	140	15	Brd + H + St
	B	60	2130	–	140	Ramp	Brd + H + St
	C	53	1950	1770	130	10	Brd + H + St + D
	D	57	2150	–	40	Ramp	Brd + H + St
MASH7-3	A	94	1975	1820	120	10	Brd + H
MASH7-4	A	112	1880	1750	80	12	Brd + H
MASH7-5	A	123	1930	1740	100	12	amorphous
MASH7-5*	A	123	1930	1740	100	12	PPv + Brd + Sf
MASH7-6	A	38	1900	1700	140	15	D + St + Brd + Cor
	B	37	1700	1610	50	20	D + St + Brd + Cor
	C	34	1590	1400	80	35	D + St + Brd + Cor
MASH7-7	A	50	1900	1790	110	15	D + St + Brd + H
	B	48	1620	1540	70	30	D + St + Brd + H
	C	45	2100	–	100	Ramp	D + St + Brd + H
MASH7-8	A	88	1700	1600	80	15	Brd + H
	B	87	2020	1800	140	10	Brd + H
MASH7-8*	A	88	1700	1600	80	15	Brd + H
	B	87	2020	1800	140	10	Brd + H
MASH7-9	B	38	2050		100	Ramp	–
	C	33	1950		100	Ramp	–
MASH7-11	A	91	2400		70	Ramp	–

Mean T and 2 s error as described in text; Ramp = ramped heating experiment.
Brd = bridgmanite; PPv = post-perovskite; Per = periclase; St = stishovite; Sf = seifertite; D = Phase D; H = Phase H; Cor = corundum.
Phases are listed according to estimated order of abundance based on the relative intensity of major diffraction peaks.
* Diffraction taken at high pressure and room temperature.

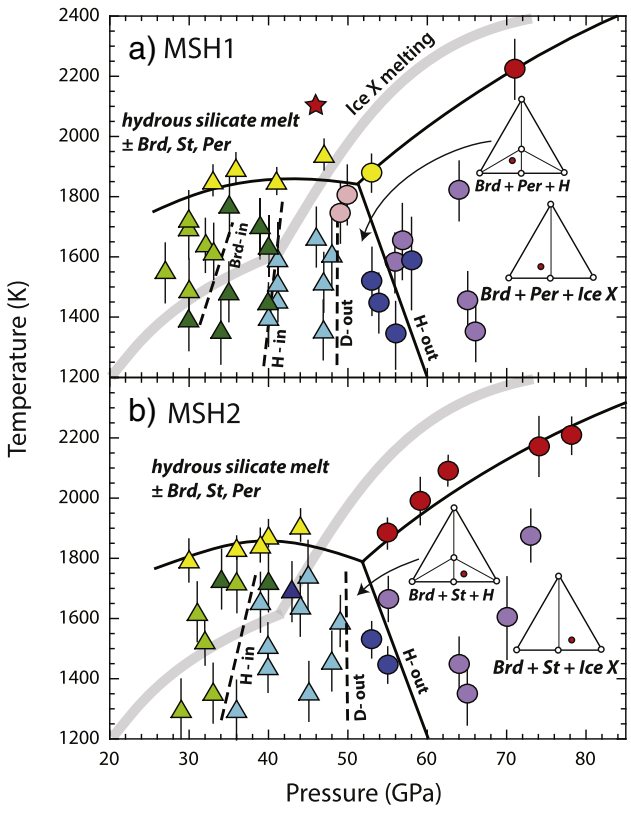

Fig. 4. Pressure–temperature diagram showing the experimental phase relations observed for compositions MSH1 (a) and MSH2 (b). Triangles represent experiments containing phase D and circles are phase D absent. Light green = D + Per + St; dark green = D + Brd + Per + St; light blue = H + D + Brd ± Per, St; dark blue = Brd + H ± St,Per; purple = Brd ± Per, St + IceX (inferred); light yellow = ramp experiments containing phase D and/or phase H; red = ramp experiments with no observable hydrous phase; pink = Brd + St + Per. The red star is a supra-liquidus experiment heated above the temperature plateau. The IceX melting curve is from Schwager and Boehler (2008). Insets show three-phase triangles in MSH as labeled in Fig. 1.

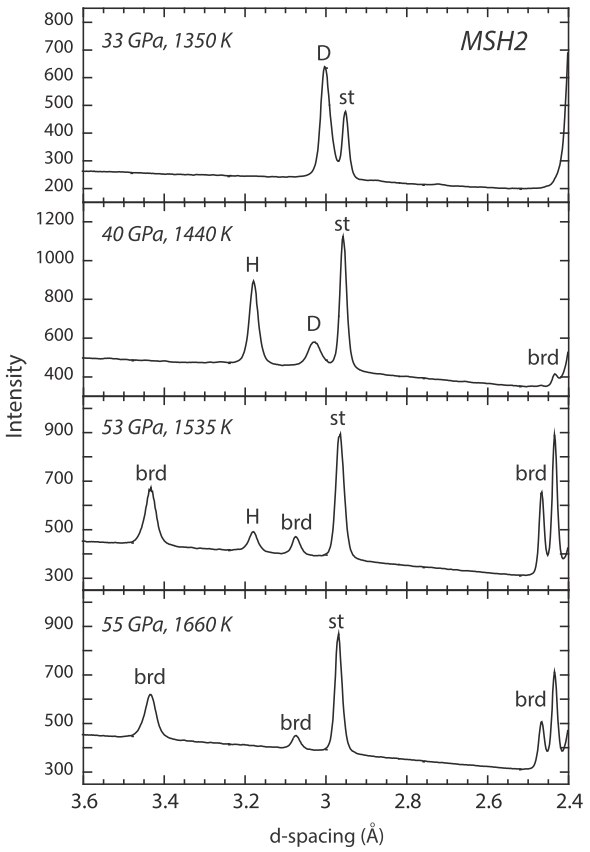

Fig. 5. Diffraction patterns of P–T quenched experiments in composition MSH2 at d-spacings in the range of 2.4–3.6 Å. Note that in addition to the phases shown, periclase occurs as a minor phase at 33 and 40 GPa, but is absent in the experiments at 53 and 55 GPa.

of brucite, which we interpret as unreacted starting material, likely at the edge of the chamber. We use the following abbreviations in discussing phase relations: Brd = bridgmanite; PPv = post perovskite phase; Per = periclase; St = stishovite; Sf = seifertite; H = phase H; D = phase D; Bru = brucite; Cor = corundum; IceX = high pressure form of water ice; Liq = liquid phase (melt or high density fluid).

3.1. Phase relations in the system MSH

Fig. 4 shows P–T plots illustrating the phase assemblages observed in diffraction measurements of quenched samples for the two bulk compositions in the MSH system. In the experiments in this system we expect no more than four phases to be present (isobaric invariance), with 3-phase assemblages most likely (isobaric univariance). The assemblages may all be solids, and potential 3-phase fields involving candidate solids are depicted in Fig. 1. Alternatively, phase relations may involve a liquid phase. At pressures of 50 GPa and above, in 24 of 25 experiments we observe either 2- or 3-phase solid assemblages. Conversely, at pressures below 50 GPa, only 11 of 49 experiments contained a 3-phase assemblage, while 18 have a 4-phase assemblage and 20 a 5-phase assemblage. We will consider the higher-pressure phase relations first.

3.1.1. Experiments at >50 GPa

Two boundaries have been located at high pressure, which produce sensible ternary phase relations. In isothermal experiments at ~1800 K and below, we bracket a boundary between phase assemblages containing phase H on the low-pressure side, to a phase H absent assemblage on the high-pressure side. On the low-pressure side of the boundary assemblages are Brd + H + Per (MSH1) or Brd + H + St (MSH2). On the high pressure side phase H disappears, and we observe 2-phase assemblages of Brd + Per or Brd + St. Diffraction spectra documenting this boundary are shown in Fig. 5, where it is clear that phase H coexists with Brd and St at 53 GPa, but is absent at 55 GPa. Mass balance requires the addition of a third, hydrous phase, and we assume that at the run conditions the H_2O component exists as phase Ice X, which on the basis of some experiments and theory, may be stable at these conditions (Schwager et al., 2004; Schwager and Boehler, 2008; Schwegler et al., 2008); when quenched to room pressure the ice phase would melt and vaporize. Three-phase triangles depicting these sub-solidus equilibria are shown as insets on Fig. 4. The phase H-out boundary occurs between 55 and 60 GPa and apparently has a negative dT/dP slope. This boundary is very close to the H-out boundary of 52 GPa predicted for $MgSi_2O_6H_2$ composition in first principles molecular dynamics calculations (Tsuchiya, 2013) (Fig. 1), and is generally consistent with recent multi-anvil results (Nishi et al., 2014), where phase H stable was found to be stable in both $MgSiH_2O_4$ and $Mg_2Si_3O_5H_2$ compositions at 50 GPa and 1273 K.

As shown on Fig. 4, the ramped experiments produce a curve with a positive dT/dP slope at pressures above 50 GPa, and the assemblages lack a hydrous phase. We and other workers have found temperature–laser power plateaux to be extremely robust indicators of melting in several metal and silicate systems (Shen and Lazor, 1995; Dewaele et al., 2007; Lord et al., 2009; Lord et al., 2010; Anzellini et al., 2013; Fischer et al., 2013; Lord et al., 2014; Thomson et al., 2014), with melting curves constrained in this way comparing well with melt detection by independent techniques, most significantly the detection of liquid diffuse scattering during in situ XRD (Dewaele et al., 2007; Anzellini

et al., 2013; Lord et al., 2014). For a more complete discussion of the evidence for the use of plateaux in power vs. temperature functions as a melting criterion, see Lord et al. (2014). Corroborating textural evidence for melting is provided below. Thus, our preliminary interpretation is that the thermal perturbations are indicative of eutectic melting in the Brd + Per + IceX and Brd + St + IceX ternaries. Our boundary falls about 200 K below the melting curve of Ice X of Schwager et al. (2004) that has been corroborated by theory (Schwegler et al., 2008), but above the lower temperature experimental determinations of two other diamond anvil cell studies (Goncharov et al., 2005; Lin et al., 2005). In contrast to our results, Nishi et al. (2014) report breakdown of phase H to an assemblage of Brd + St + fluid or Brd + fluid in experiments at 1373 K, suggesting that this represents the dehydration/melting temperature of phase H. This is hard to reconcile with our observations of phase H present to temperatures of the order 1600 K at 54 GPa.

3.1.2. Experiments at <50 GPa

At pressures less than 50 GPa phase relations in MSH are more challenging to interpret. However, several boundaries are apparent in the data that are consistent in both starting compositions. The first appearance of phase H in MSH1 composition is tightly bracketed at ~ 40 GPa, and in composition MSH2 phase H appears at somewhat lower pressures, in the range of 35 to 40 GPa. Fig. 5 shows diffraction data that clearly indicate the emergence of phase H at 40 GPa in composition MSH2, whereas it is absent in the experiment at 33 GPa. These results are generally consistent with those of Nishi et al. (2014) who found phase H present in the endmember composition at pressures as low as 35 GPa. The next obvious boundary in our experiments is a phase D-out boundary that occurs at ~48 GPa in both compositions. This boundary is very close to the phase-D out boundary found by Nishi et al. (2014) in multi-anvil experiments at 1273 K, is generally consistent with the DAC observations of Shieh et al. (1998) on a natural lizardite composition, and is close to the boundary based on molecular dynamics calculations (Tsuchiya, 2013). We note that phase H and phase D coexist in most of our experiments between the H-in and D-out boundaries, and that these experiments tend of have 4 to 5 phases (Brd + H + D ± Per ± St).

A five-phase assemblage would require P–T invariance, and because we observe this over a range of conditions we interpret this violation of the phase rule as disequilibrium. This might be explained as a consequence of the bulk compositions being relatively close to 3-phase triangles involving D + H + Per and Brd + H + D (Fig. 2). Another possibility is that a liquid phase is present, and that thermally induced chemical segregation, either Soret or saturation gradient diffusion (Lesher and Walker, 1988; Sinmyo and Hirose, 2010), leads to complex dis-equilibrium assemblages. This effect could be significant especially in regions of the phase diagram where multiple reactions occur over a relatively narrow P–T–X range. However, the observed consistency of our phase-in and phase-out boundaries, combined with results from other independent methods, lends credence to these multi-phase assemblages in locating primary phase boundaries.

In isothermal experiments at pressures less than ~35 to 40 GPa, we consistently produce the univariant assemblage D + St + Per in both starting compositions. Fig. 5 shows an example of an unequivocal diffraction pattern from an MSH2 experiment at 33 GPa, 1350 K, showing phase D and stishovite but no bridgmanite. Fig. 6a shows a false-color X-ray map of a polished MSH2 sample from an experiment at 36 GPa and 1710 K, which exhibits a generally uniform and well-crystallized mixture of phase D, stishovite and periclase. We can identify a Brd-in boundary at ~35 GPa and 1600 K, best constrained in MSH1 composition. The absence of bridgmanite was also observed in the DAC experiments of Shieh et al. (1998) on a lizardite composition at similar conditions, although those workers observed Brd-in at somewhat higher pressures. In contrast, Nishi et al. (2014) produce a Brd + St + Liq assemblage at 1673 K in a phase D bulk composition at 25 GPa, Recently, Ghosh and Schmidt (2014) found that phase D

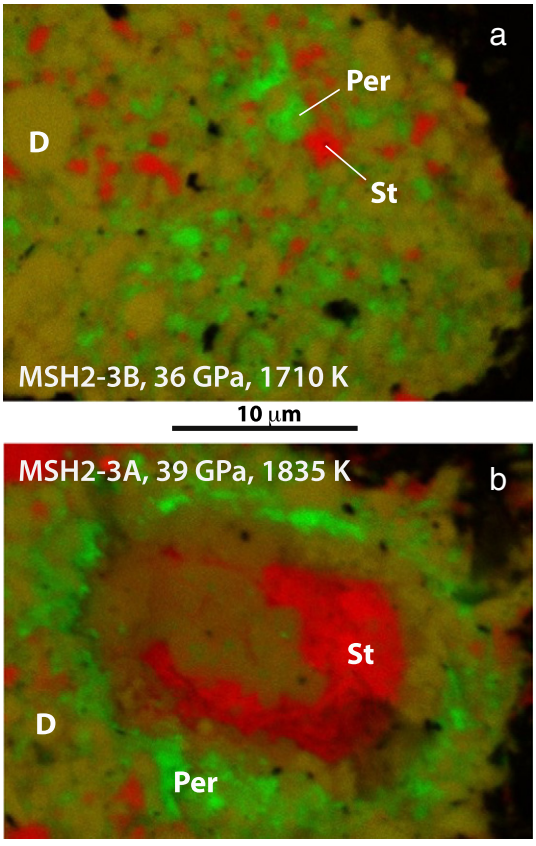

Fig. 6. False-color X-ray intensity images obtained using a JEOL field-emission electron microprobe at the University of Bristol on run products from experiment MSH2–3. Red = Si; Green = Mg. Frame (a) shows a run product heated isothermally at 1710 ± 50 K and (b) shows a ramped experiment with a plateau at 1835 K. The 'bulls-eye' texture is commonly observed in ramped-style melting experiments, in contrast to uniform textures typically observed in isothermal experiments. Probe conditions were 10 nA beam current with an 8 kV accelerating potential.

coexists with Brd + St + Mg-rich hydrous melt at 24 GPa, 1623 and 1648 K, in a Si-rich bulk composition in the MSH system; they interpreted this four-phase assemblage to represent spanning of a phase boundary in a temperature gradient, rather than isobaric invariance, and place the solidus at ~1623 to 1648 K. At 32 GPa, 1673 K, these workers find that a Mg-rich hydrous melt coexists with Brd + St, and their results are generally consistent with the phase relations predicted by Komabayashi et al. (2004) at these conditions.

Taken at face value, the assemblage D + St + Per could be stable if a 3-phase triangle exists between periclase, phase D and stishovite. This could arise if stishovite becomes sufficiently hydrated (Spektor et al., 2011) such that a tie-line emerges between periclase and stishovite that occludes anhydrous Brd (Fig. 1), and would explain the repeated appearance of this assemblage in both Mg-rich (MSH1) and Si-rich (MSH2) compositions. Another possibility is that the assemblage occurs due to the involvement of a liquid phase, for example in the reaction:

$$D + Brd = St + MgO\text{-rich liquid}.$$

As noted above, Ghosh and Schmidt (2014) found that an MgO-rich hydrous liquid coexists with bridgmanite ± phase D in the MSH system at pressures of 24 and 32 GPa. Further, first principles molecular dynamics calculations indicate complete miscibility of water and silicate melt throughout almost the entire mantle pressure regime, and note a strong preference for water molecules to bond with Mg cations (Mookherjee et al., 2008). However, why bridgmanite should be absent in our bulk

compositions is unclear, as chemography indicates that bridgmanite should not be the first phase exhausted in such a reaction (Fig. 1).

The ramped experiments at pressures between about 30 and 50 GPa produce relatively flat curves in both starting compositions at ~1800 K. Fig. 6b shows a false-color X-ray map of a ramp experiment at 39 GPa that exhibited a clear temperature plateau at ~1835 K. Compared to the uniform texture observed in the isothermal experiment at 1710 K (Fig. 6a), a distinctly non-uniform, 'bulls-eye' texture developed in this experiment. We commonly observe this kind of texture in ramp-type experiments in MSH, typically showing a concentration of stishovite in the center. This might represent the reaction given above where stishovite crystallizes upon melting due to a very Mg-rich hydrous melt. The periclase-rich annulus surrounding the mixed D + St region in Fig. 6b could represent quenched Mg-rich hydrous melt, and further analyses are required to test this hypothesis.

When combined with the curve derived from the ramped experiments at higher pressures, an inflection is apparent that correlates well with the intersection of the H-out boundary (Fig. 4), and such an inflection is expected where a subsolidus reaction intersects a melting curve. As with the higher-pressure experiments, our current interpretation based on the temperature plateaus and textural evidence is that this curve represents dehydration melting, and above this curve only anhydrous phases plus a hydrous silicate melt are present. The ramp experiments contain hydrous phases, which likely is a consequence of the relatively large temperature gradient. However, we note that in an experiment taken to several hundred degrees above the melting curve (red star in Fig. 4), an entirely anhydrous solid assemblage was produced.

3.2. Phase relations in the system MASH

Fig. 7 is a P–T plot showing the phase assemblages observed in diffraction measurements from quenched samples for the five bulk compositions in the MASH system. The addition of alumina to the MSH system creates solid solutions in bridgmanite, phase D and phase H, and to a minor extent in stishovite. A complete solid solution between endmember $MgSiH_2O_4$ and AlOOH may exist (Fig. 1). However, for convenience we will continue to refer to the (Mg,Si,Al)OOH solid solution as phase H. Because of the solid solutions in the MASH system, three-phase equilibria are expected to dominate sub-solidus phase relations, and of the 56 experiments on which diffraction data were collected, 31 have three phases, 17 have four phases and 3 have 5 phases.

3.2.1. Subsolidus phase relations

In contrast to the results in the MSH system, we find that bridgmanite is stable in all experiments in the MASH system, with the exception of one at 123 GPa where it is replaced by post-perovskite. At pressures less than ~45 GPa the subsolidus assemblage is Brd + D + St or Per, depending on the bulk composition, although minor corundum was apparent in a few of the lower pressure run products. The first appearance of phase H occurs at ~45 GPa, and most of the experiments with 4 or 5 phases occur between ~45 and 55 GPa and define a region wherein aluminous phase D and phase H solid solutions coexist. As shown by the diffraction patterns in Fig. 8, an experiment at 49 GPa and 1755 K produced an assemblage of Brd + D + H + St in composition MASH3, but by 62 GPa phase D is absent. A phase D-out boundary is constrained by all compositions at ~55 to 60 GPa, or about 5 to 10 GPa higher than observed in the MSH system. The data indicate that phase D is stabilized in the alumina-bearing system to higher pressures than in the MSH system. Above ~60 GPa phase H solid solution is the stable hydrous phase, coexisting with bridgmanite and a free silica phase in SiO_2-rich compositions, or with bridgmanite plus periclase in MgO-rich compositions. Our data show phase H stable in the quenched products of all experiments up to 116 GPa. Thus, even the addition of as little as ~2.5 mol% alumina

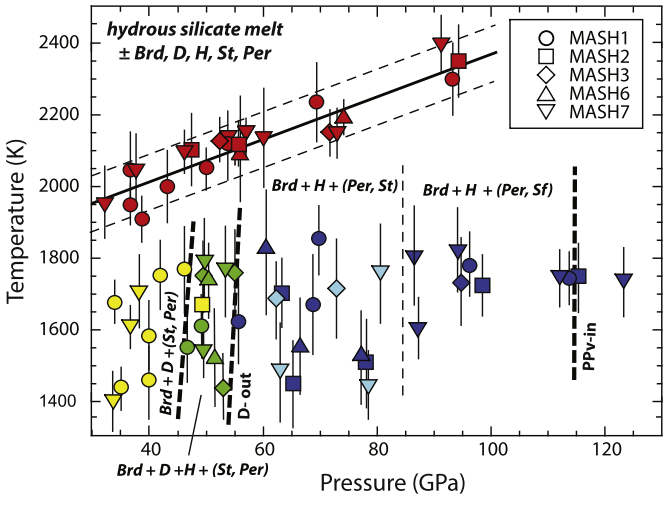

Fig. 7. Pressure–temperature diagram showing the experimental phase relations observed for compositions in the MASH system. Symbol shapes correspond to different bulk compositions as shown in the legend. Symbol colors are as follows: yellow = phase D-bearing but phase H absent; light green = phase D and H coexisting in the assemblage; light blue = Brd + H + St; dark blue = Brd + H ± Per; red = ramped experiments. The melting curve is defined as a linear fit to the data, with a slope of 6.1 K/GPa, and the thin dashed lines show 2σ uncertainty on the fit. Phase labels as in Fig. 1.

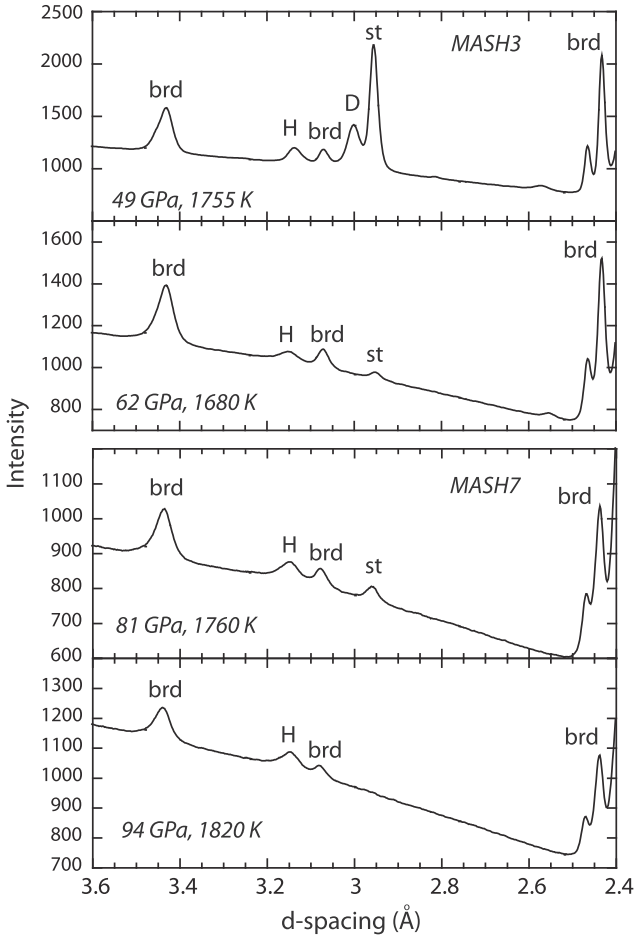

Fig. 8. Diffraction patterns of P–T quenched experiments in the MASH system at d-spacings in the range of 2.4–3.6 Å. Note that in addition to the phases shown, periclase occurs in the experiments on composition MASH2, but is absent in the experiments on MASH7. Phase labels as in Fig. 1.

to the MSH system appears to stabilize a phase H solid solution to the base of the lower mantle.

In experiment MASH2-4 we observe an assemblage of bridgmanite, post-perovskite and periclase in a diffraction pattern taken at 116 GPa (300 K). The post-perovskite diffraction lines are well fitted, but are weak relative to the bridgmanite lines. In contrast, in MASH7-5 at 123 GPa the post-perovskite lines are strong relative to weaker bridgmanite lines. These observations indicate that at ~1800 K post-perovskite stabilizes in the region of 115 GPa in a composition with ~5 mol% Al_2O_3, and that in a composition with ~10 mol% Al_2O_3 bridgmanite-out will occur in the region of 130 GPa. Bridgmanite and post-perovskite will coexist in a two-phase loop with the addition of alumina to the $MgSiO_3$ system. Previous experimental results indicate that bridgmanite is stabilized to higher pressures with addition of alumina, and that the two-phase region is large for the composition $MgSiO_3$–25 mol% Al_2O_3, extending to greater than ~150 GPa (Tateno et al., 2005). First principles calculations confirm that bridgmanite is stabilized relative to post-perovskite, and for compositions in the range of 5–10 mol% Al_2O_3, 2-phase loops of ~10–20 GPa width are predicted (Akber-Knutson et al., 2005). We tentatively put the position of the post-bridgmanite in boundary at ~115 GPa based on experiment MASH2-4 with ~5 mol% Al_2O_3. This is close to the boundary predicted for pure $MgSiO_3$ (Murakami et al., 2004; Ono and Oganov, 2005), however, as our pressures do not include a thermal term, we likely underestimate pressure of the phase boundary, perhaps by as much as 10%, and so the boundary is more likely to occur at ~125–130 GPa at high temperature. Our data indicate a relatively narrow two-phase region, of the order 10–20 GPa, which is close to the ab initio predictions but considerably narrower than previous experimental results in the MAS system. We note that phase H was not unambiguously identified in the high pressure patterns, but was clearly present in the quenched pattern from 115 GPa. With the exception of Pt and Re, no diffraction lines were evident in the quench product of the 123 GPa experiment, indicating that all phases became amorphous upon pressure release.

At pressures above ~90 GPa, we no longer observe the presence of stishovite in the quenched diffraction patterns in Si-rich bulk compositions (Fig. 8); all peaks can be indexed with bridgmanite plus phase H. Chemographically, excess silica must be balanced by a silica-rich phase. However, we note that in the high pressure pattern on sample MASH7-5 at 123 GPa (300 K), a full profile fit is achieved with a combination of post-bridgmanite, bridgmanite and seifertite, a high-pressure form of SiO_2 known to be stable in this pressure range (Grocholski et al., 2013). It may be that hydrous and aluminous seifertite is not quenchable, in which case it could be present in all of the apparently stishovite-free experiments above 90 GPa in SiO_2-rich compositions. This is generally consistent with the stishovite to seifertite phase boundary observed by Grocholski et al. (2013).

3.2.2. Melting systematics

The ramped experiments in the MASH system produce a curve with a positive dT/dP slope (~6 K/GPa). Within uncertainty we cannot detect a difference in the melting temperatures related to bulk composition. We suggest that this curve represents the upper temperature limit of hydrous phase stability of phases D or H depending on pressure. Because solid solutions are involved, these phases may persist above the solidus over some temperature range, in which case our method of melt detection may overestimate the solidus temperatures. Indeed, in all the ramped experiments where we have diffraction data, either phase D or H are present. However, as these experiments were quenched while on a temperature plateau, and experimental temperature gradients certainly spanned solidus temperatures, the presence of a hydrous phase in the diffraction pattern is not unexpected. Similar to the MSH system, we typically observe uniform textures in sub-solidus experiments, which we find readily amenable to mechanical polishing. However, melting experiments commonly exhibit a friable, difficult to polish core region, which we interpret as the partially melted region.

When compared to the melting curve in the MSH system, we find that the MASH curve is several hundred degrees above the MSH curve at less than ~60 GPa. In the MASH system the melting curve has a shallower slope than in MSH at higher pressures, apparently due to the high pressure stability of phase H, and the two curves are close in temperature at ~90 to 100 GPa. Our observed position of the solidus temperature in the MASH system at ~30 GPa, and the increase in the solidus by ~200 K relative to MSH, are generally consistent with the multi-anvil results of Ghosh and Schmidt (2014), and indicate that addition of alumina to phase D significantly increases the melting temperature (Pamato et al., 2015).

3.3. Unit cell volumes, phase compositions and mass balance

Bridgmanite and phases D and H can all exhibit considerable alumina solution, with more than 25 mol% Al_2O_3 stable in the bridgmanite structure in MAS at lower mantle pressures (Walter et al., 2004; Walter et al., 2006), and potentially complete solid solutions between MgSi- and Al-end-members in phases D and H (Ohira et al., 2014; Pamato et al., 2015). Our attempts to measure crystal compositions directly in experiments in the MASH system with the field emission gun electron microprobe yielded analyses of phase mixtures due to their sub-micron size, which is consistent with the crystal sizes observed in the experiments of Ohira et al. (2014). Unit cell volumes of a P–T quenched phase can in some cases be used to estimate phase compositions at the experimental synthesis conditions (Mao et al., 1991; Walter et al., 2004). A relatively simple linear relationship between ambient unit cell volume and composition is apparent for alumina-bearing bridgmanite in the MAS system (Walter et al., 2004; Walter et al., 2006), and so may be useful to estimate bridgmanite compositions in our experiments.

We calculated unit cell volumes for bridgmanite in experiments in both the MSH and MASH system throughout the covered pressure range, and the results are provided in Table 4 and shown in Fig. 9. We were typically able to use a dozen or more reflections for volume calculations, resulting in reasonably high precision, but unfortunately, uncertainty in the volumes of phases D, H and stishovite are too large for meaningful attempts to estimate compositions, as we typically had 5 or fewer usable reflections for these phases.

Fig. 9 indicates that at pressures below about 55 GPa in the MASH system, where phase D is stable, bridgmanite has a relatively low alumina content, perhaps about 2 mol% Al_2O_3 when cast in the system $MgSiO_3$–Al_2O_3. At higher pressures where phase H replaces phase D as the hydrous phase, there is a continuous increase in the unit cell volume of bridgmanite with synthesis pressure, suggesting that the amount of alumina in bridgmanite coexisting with phase H increases with pressure. For example, on the basis of this interpretation we would predict that at 70 GPa bridgmanite contains about 6–7 mol% alumina, and at 100 GPa about 10 mol% alumina. Unit cell volumes do not appear to systematically vary with bulk composition as expected, which could mean the dependence is small relative to the uncertainty in the cell volumes.

Estimating bridgmanite alumina content on the basis of Fig. 9 permits mass balance calculations against system bulk compositions. For three-phase sub-solidus equilibrium among Brd + D + (Per, St) at lower pressures, or Brd + H + (Per, St) at higher pressures, the composition of phases D and H can be uniquely defined if the compositions of the coexisting phases are fixed. Using compositions MASH1 (Mg-rich, Al-poor) and MASH7 (Si-rich, Al-rich) as examples, we made mass balance calculations on the basis of the inferred bridgmanite compositions from Fig. 9.

For MASH1 composition at low pressures, and estimating 2 mol% Al_2O_3 in bridgmanite, mass balance yields 78% brd + 14% D + 8% per, with phase D containing ~12 mol% Al_2O_3. This indicates that Al partitions strongly into phase D relative to bridgmanite. The same calculation for MASH7 does not yield a three-phase solution involving Brd + D + St, but requires excess Al_2O_3 for mass balance. Indeed,

Table 4
Unit cell volume of bridgmanite at 1 atm, 300 K.

Experiment	Hole	P (GPa)	Mean T (K)	(Å3)	σ
MSH1-9	A	58	1590	162.35	0.051
	B	53	1520	162.13	0.042
	C	54	1450	162.55	0.053
	D	56	1350	162.39	0.071
MSH1-11	A	65	1450	161.78	0.042
	B	66	1350	162.39	0.051
	C	56	1575	162.37	0.063
	D	57	1650	162.43	0.058
MSH2-9	B	49	1585	162.29	0.112
	C	48	1450	162.33	0.061
	D	45	1350	162.66	0.113
MSH2-10	A	70	1600	162.26	0.037
	B	64	1450	162.14	0.042
	C	65	1350	161.88	0.110
MASH1-1	A	68	1670	162.930	0.063
	C	70	1850	163.100	0.074
MASH1-2	A	56	1620	162.450	0.082
	C	53	1605	162.800	0.151
MASH1-3	A	96	1780	163.480	0.110
MASH1-5	A	46	1760	162.330	0.106
	B	47	1550	162.560	0.150
MASH1-6	B	34	1670	162.710	0.083
	C	35	1440	162.800	0.121
MASH1-7	A	42	1750	162.550	0.120
	B	40	1580	162.740	0.100
	C	40	1460	162.810	0.085
MASH2-1	A	78	1510	163.350	0.075
	B	62	1700	162.890	0.066
	C	65	1450	162.990	0.051
MASH2-2	D	51	1670	162.790	0.100
MASH2-3	A	98	1720	163.940	0.067
MASH2-4	A	116	1750	163.95	0.223
MASH3-1	B	62	1680	162.980	0.076
	C	73	1710	162.900	0.105
MASH3-2	A	55	1750	162.780	0.107
	C	53	1435	162.770	0.086
	D	49	1755	162.660	0.120
MASH3-3	A	95	1730	163.65	0.083
MASH6-1	A	77	1525	163.020	0.064
	B	66	1550	163.100	0.130
MASH6-2	A	50	1740	162.770	0.122
	B	60	1825	162.620	0.107
	D	51	1515	162.710	0.094
MASH7-1	A	81	1760	163.110	0.211
	B	78	1450	162.960	0.073
MASH7-2	A	63	1490	162.690	0.100
	C	53	1770	162.600	0.122
MASH7-3	A	94	1820	163.350	0.111
MASH7-6	B	37	1610	162.660	0.324
	C	34	1400	162.350	0.198
MASH7-7	A	50	1790	162.480	0.140
	B	48	1540	162.470	0.200
MASH7-8	A	88	1600	163.660	0.300
	B	87	1800	163.510	0.140

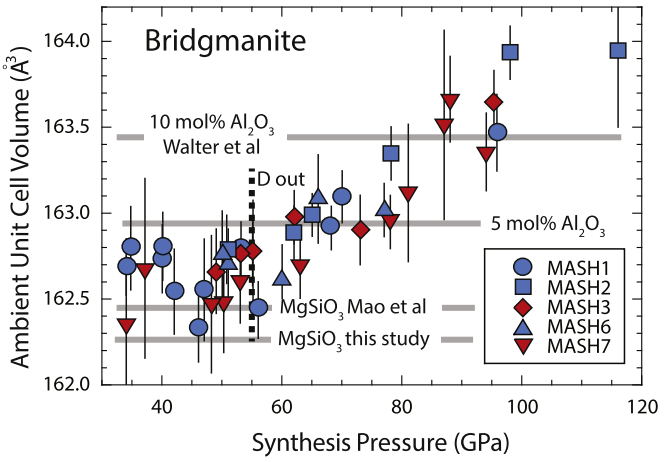

Fig. 9. Ambient (1 atm, 300 K) unit cell volumes of bridgmanite in experiments in the MASH system as a function of synthesis pressure (see Table 4). Symbol shapes correspond to starting compositions. Blue = Mg-rich compositions; Red = Si-rich compositions. Ambient P–T volumes in the $MgSiO_3$ (Mao et al., 1991; this study) and $MgSiO_3$–Al_2O_3 systems (Walter et al., 2004) are shown as gray contours.

experiment MASH7-6 (Table 3) at ~35 GPa produces this assemblage. The composition of coexisting phase D cannot be constrained in this case as there is a range of possible compositions that yield 4-phase solutions.

We repeated this exercise using an estimated bridgmanite composition of 7 mol% Al_2O_3 at 70 GPa. For composition MASH7, mass balance yields 84% Brd + 12% H + 4% St, and a phase H composition with ~40 mol% Al_2O_3 ($[Mg_{10}Al_{80}Si_{10}]SiH_2O_4$). The results of Ohira et al. (2014) are generally consistent with these findings. These workers quantified phase compositions using TEM analyses of phases in an experiment at 68 GPa in a highly aluminous starting composition in the system $MgSiO_3$–Al_2O_3–H_2O. They found that bridgmanite contains about 6 mol% Al_2O_3 and coexists with phase H containing about 30 mol% Al_2O_3. Further support for aluminous phase H in our experiments comes from the d-spacing of the (110) phase H reflection. The average d-spacing of this reflection in our MASH experiments is 3.15 ± 0.01 Å. Literature data shows that highly aluminous phase H and endmember δ-AlOOH have (110) d-spacings in the range of ~3.14–3.15 Å, whereas the d-spacing in endmember $MgSiH_2O_4$ in our MSH experiments is 3.176 ± 0.002 Å, and was measured to be 3.19 Å by Bindi et al. (2014).

While perfectly reasonable 3-phase mass balance can be achieved for a range of bridgmanite compositions, as in the examples above, 3-phase mass balance cannot be achieved in bulk compositions MASH1 and MASH3 if bridgmanite contains more than ~5 mol% Al_2O_3 ($MgSiO_3$–Al_2O_3), above ~8 mol% Al_2O_3 for composition MASH2, and above ~10 mol% Al_2O_3 for compositions MASH6 and MASH7. Thus, at the highest pressures the observed unit cell volumes indicate alumina contents in bridgmanite that are too high for successful mass balance with the system bulk compositions; a fourth, alumina-poor phase is required for mass balance, which is not observed.

The failure in mass balance at high pressures requires an alternative explanation for the observed positive correlation between cell volume and synthesis pressure in Fig. 9. One possibility is that the volume increase with pressure is a quench phenomenon related to decompression. We find this unlikely, as the ambient unit cell volume of bridgmanite in the MSH experiments shows no correlation with pressure, with an average value of 162.3 ± 0.2 $Å^3$.

A second possibility is that the increase in cell volume is not related to alumina incorporation alone, but also reflects addition of hydrogen into the bridgmanite structure. Measurements of hydrogen in bridgmanite synthesized experimentally in hydrous systems, using both infrared spectroscopy and secondary ion mass spectrometry, have yielded a puzzling range of values from undetectable to several thousand ppm (Bolfan-Casanova et al., 2000; Murakami et al., 2002; Litasov et al., 2003; Bolfan-Casanova, 2005). Recent ab initio calculations in which the partition coefficient of hydrogen between hydrous ringwoodite and bridgmanite in $MgSiO_3$ was determined indicate as much as a thousand ppm H in bridgmanite (Hernandez et al., 2013).

Substitution of hydrogen into bridgmanite may be enhanced by coupled substitution of Al^{3+} on the octahedral site through charge balance: $Si^{4+} = Al^{3+} + H^+$. This can occur in a variety of ways, one of which is through the formation of an oxygen vacancy and subsequent protonation: $V_o^0 + O_o^{2-} + H_2O = 2OH^-$ (Navrotsky, 1999; Brodholt, 2000; Navrotsky et al., 2003). However, oxygen vacancy formation of this sort has been shown to be generally unfavorable in bridgmanite at lower mantle pressures, and should become less favorable with increase in pressure (Brodholt, 2000; Walter et al., 2006). Another

mechanism would be direct incorporation of an $MgAlHO_3$ component, with protonation of oxygen near to Al^{3+} on the octahedral site. Addition of hydrogen to the bridgmanite structure is expected to increase the unit cell volume, perhaps at a higher rate than for Al^{3+} alone, and this is a possible explanation for the trend observed in Fig. 9. If this interpretation were correct, then the alumina content may remain relatively low in bridgmanite throughout the lower mantle, with alumina preferentially partitioning into phase H. This might also indicate the potential for substantial hydrogen solution in bridgmanite, with important implications for the water storage capacity of the lower mantle. Further investigation is needed to test this hypothesis.

4. Discussion

Our results show that in the MASH system, a stable hydrous solid phase can be stable in the subsolidus of model peridotitic and basaltic compositions throughout the lower mantle pressure range; phase D in the shallow lower mantle and phase H from the mid-lower mantle to the mantle–core boundary. In the MSH system, phase D is stable to about 45 GPa, where it is replaced by the endmember phase H, $MgSiH_2O_4$, and phase H has a high-pressure stability limit of ~55 GPa. In the MASH system an aluminous (Mg,Si,Al)OOH solid solution appears at ~45 GPa in both model peridotitic and basaltic bulk compositions, and remains stable in the subsolidus throughout the lower mantle pressure range. Thus, depending on temperature, phase H is potentially an important host for water in the deep lower mantle (Ohira et al., 2014).

Fig. 10 shows a P–T diagram summarizing our results relative to the trajectories of model ambient mantle and cold subduction geotherms. Geotherms for lithosphere subducted into the lower mantle are poorly constrained, and extrapolation of thermal models made for the upper mantle yield a wide range of possible trajectories (Kirby et al., 1996; Eberle et al., 2002; Syracuse et al., 2010). The slab geotherm shown on Fig. 10 represents the coldest portion of the slab in the model of Kirby et al. (1996), extrapolated to the base of the mantle, and this profile probably represents a minimum. Along this model subduction geotherm we expect an aluminous hydrous phase, either D or H, to be stable in hydrated, subducted lithosphere throughout the lower mantle depth range (Ohira et al., 2014). We also plot a model ambient mantle geotherm on Fig. 10 for the lower mantle, assuming a temperature of 1900 K at 660 km (Brown and Shankland, 1981; Ito and Katsura, 1989).

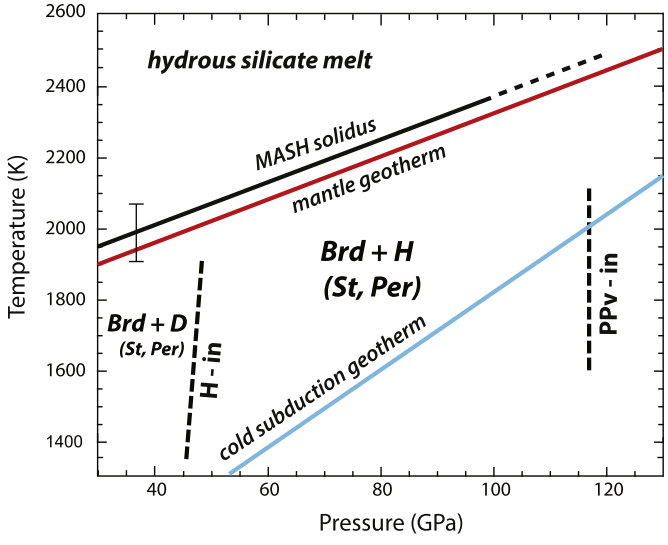

Fig. 10. Pressure–temperature diagram summarizing the results of this study. Subsolidus phase boundaries are estimated on the basis of experiments in the MASH system. The red line shows an estimate of an adiabatic lower mantle geotherm based on a temperature of 1900 K at the 660 km discontinuity (e.g., Ito and Katsura, 1989), and based on the adiabatic gradient from Brown and Shankland (1981). The blue line shows a model cold slab geotherm from Kirby et al. (1996), which probably represents a minimum for subducting slabs in the lower mantle.

Ghosh and Schmidt (2014) observed a high temperature stability limit for aluminous phase D coexisting with bridgmanite of ~1900 K at 24 GPa in the MASH system, although a hydrous Mg-rich melt is also present at temperatures as low as ~1600 K. This is generally consistent with the results of Schmandt et al. (2014), who found melt present upon heating of hydrous ringwoodite to ~1900 K at 30 GPa. Ghosh and Schmidt (2014) suggest that heating of slabs that stall at the base of the transition zone or in the shallow lower mantle should lead to melting and release from the slab of a Mg-rich hydrous melt. Schmandt et al. (2014) suggest that the observed decreases in seismic velocities in regions of downwelling mantle are consistent with the presence of partial melt. Both these studies suggest that hydration of the transition zone may occur by hydrous slab melting in this depth range. Thus, it would seem that transport of water into the deep lower mantle requires either direct slab penetration into the lower mantle along a cold slab geotherm, or that aluminous phase D remains stable in the presence of hydrous melting around the 660 km discontinuity, such that some hydrous component can be delivered to the lower mantle upon further subduction. Ohira et al. (2014) suggest that hydrous melts might become trapped in subducting material due to their poor wetting properties, and be delivered to the lower mantle where the hydrous component would be stored in phase H.

The curve that we interpret as dehydration melting in the MASH system is very close to the model mantle geotherm on Fig. 10. However, because the mantle will have other components that will lower the melting temperature relative to the MASH system (e.g., Fe, Ca, Na, K), we predict that a solid hydrous phase will not be stable in the ambient lower mantle, and that when the storage capacity for hydrogen in bridgmanite is exceeded, a hydrous silicate liquid will be stable throughout the lower mantle along an adiabatic geotherm. If a subducting slab carries hydrogen in phase H to the deep lower mantle, perhaps all the way to the core–mantle boundary region, and then heats up toward ambient mantle temperatures, it will eventually melt and a hydrous silicate liquid will be stable. Likewise, any primordial hydrogen in the deep lower mantle after accretion would be expected to lead to melting. The calculations of (Mookherjee et al., 2008) are suggestive that melts at these deep lower mantle conditions may be neutrally or negatively buoyant relative to solid mantle, and so could become trapped. The expected small volume fraction of hydrous melt would not likely have a detectable effect on observed isotropic seismic velocity in the lower mantle. However, the lowermost mantle has a strong, heterogeneous seismic anisotropy, and the anisotropic signature of large low shear-velocity provinces, especially in the D″ region, appears to be distinct from that of other parts of the lowermost mantle, for example beneath subduction zones (Nowacki et al., 2010; Cottaar and Romanowicz, 2013; Nowacki et al., 2013). A candidate for producing seismic anisotropy is the presence of aligned melts, as these can have a strong anisotropic signature even in small volume fractions (Kendall and Silver, 1996). This possibility should be considered in seismic models of deep mantle anisotropy as our results suggest that along a mantle geotherm a hydrous silicate melt will be stable, and is likely to be the host for hydrogen in the deep lower mantle.

5. Conclusions

Experimentally determined phase relations in the systems MSH and MASH constrain the high-pressure stability of hydrous silicates. At ~1700 K, the recently discovered phase H appears at ~40 GPa in the MSH system, but it has a narrow stability range as predicted by ab initio calculations, with Phase H-out by ~50 GPa. However, the addition of alumina to the system vastly increases the stability of phase H, and an aluminous phase H coexisting with relatively Al-poor bridgmanite can be stable to the base of Earth's lower mantle. We suggest that the high temperature stability of lower mantle solid hydrous silicates (D and H) is defined by dehydration melting curves, which we deduce from

thermal signal processing in laser-heating experiments. On this basis we predict that lithosphere along a subduction geotherm, basaltic or peridotitic in composition, can transport hydrogen into the deep lower mantle in solid, dense hydrous silicates. However, we predict that along an adiabatic mantle geotherm that solid hydrous silicates are not stable, but that hydrous silicate melt will host hydrogen at all lower mantle depths. Understanding the nature of hydrous silicate melts in the deepest mantle, including their composition, density and wetting properties, may ultimately hold the key to modeling the behavior of hydrogen in Earth's deepest mantle.

Acknowledgments

We thank Ben Russell for help in preparing the starting compositions, and Ben Buse for assistance with FEG microprobe measurements. This work is funded by NERC grant NE/H006362/1 to Walter, with diffraction measurements at the Diamond Light Source made under awards EE8669 and EE9788.

References

Akahama, Y., Kawamura, H., 2010. Pressure calibration of diamond anvil Raman gauge to 410 GPa. International Conference on High Pressure Science and Technology, Joint Airapt-22 and Hpcj-50, p. 215.
Akber-Knutson, S., Steinle-Neumann, G., Asimow, P.D., 2005. Effect of Al on the sharpness of the $MgSiO_3$ perovskite to post-perovskite phase transition. Geophys. Res. Lett. 32 (14).
Anzellini, S., Dewaele, A., Mezouar, M., Loubeyre, P., Morard, G., 2013. Melting of iron at Earth's inner core boundary based on fast X-ray diffraction. Science 340 (6131), 464–466.
Belonoshko, A.B., Dubrovinsky, L.S., 1997. A simulation study of induced failure and recrystallization of a perfect MgO crystal under non-hydrostatic compression: application to melting in the diamond-anvil cell. Am. Mineral. 82 (5–6), 441–451.
Bina, C.R., Navrotsky, A., 2000. Possible presence of high-pressure ice in cold subducting slabs. Nature 408 (6814), 844–847.
Bindi, L., Nishi, M., Tsuchiya, J., Irifune, T., 2014. Crystal chemistry of dense hydrous magnesium silicates: the structure of phase H, $MgSiH_2O_4$, synthesized at 45 GPa and 1000 degrees C. Am. Mineral. 99 (8–9), 1802–1805.
Bolfan-Casanova, N., 2005. Water in the Earth's mantle. Mineral. Mag. 69 (3), 229–257.
Bolfan-Casanova, N., Keppler, H., Rubie, D.C., 2000. Water partitioning between nominally anhydrous minerals in the $MgO–SiO_2–H_2O$ system up to 24 GPa: implications for the distribution of water in the Earth's mantle. Earth Planet. Sci. Lett. 182 (3–4), 209–221.
Brodholt, J.P., 2000. Pressure-induced changes in the compression mechanism of aluminous perovskite in the Earth's mantle. Nature 407 (6804), 620–622.
Brown, J.M., Shankland, T.J., 1981. Thermodynamic parameters in the Earth as determined from seismic profiles. Geophys. J. R. Astron. Soc. 66 (3), 579–596.
Cottaar, S., Romanowicz, B., 2013. Observations of changing anisotropy across the southern margin of the African LLSVP. Geophys. J. Int. 195 (2), 1184–1195.
Dewaele, A., Mezouar, M., Guignot, N., Loubeyre, P., 2007. Melting of lead under high pressure studied using second-scale time-resolved X-ray diffraction. Phys. Rev. B 76 (14).
Dorogokupets, P.I., Dewaele, A., 2007. Equations of state of MgO, Au, Pt, NaCl-B1, and NaCl-B2: internally consistent high-temperature pressure scales. High Pressure Res. 27 (4), 431–446.
Eberle, M.A., Grasset, O., Sotin, C., 2002. A numerical study of the interaction between the mantle wedge, subducting slab, and overriding plate. Phys. Earth Planet. Inter. 134 (3–4), 191–202.
Elkins-Tanton, L.T., 2008. Linked magma ocean solidification and atmospheric growth for Earth and Mars. Earth Planet. Sci. Lett. 271 (1–4), 181–191.
Fischer, R.A., et al., 2013. Phase relations in the Fe–FeSi system at high pressures and temperatures. Earth Planet. Sci. Lett. 373, 54–64.
Ghosh, S., Schmidt, M.W., 2014. Melting of phase D in the lower mantle and implications for recycling and storage of H_2O in the deep mantle. Geochim. Cosmochim. Acta 145, 72–88.
Goncharov, A.F., et al., 2005. Dynamic ionization of water under extreme conditions. Phys. Rev. Lett. 94 (12).
Grocholski, B., Shim, S.H., Prakapenka, V.B., 2013. Stability, metastability, and elastic properties of a dense silica polymorph, seifertite. J. Geophys. Res. B 118 (9), 4745–4757.
Halliday, A.N., 2013. The origins of volatiles in the terrestrial planets. Geochim. Cosmochim. Acta 105, 146–171.
Hammersley, A.P., et al., 1995. Calibration and correction of distortions in 2-dimensional detector systems. Rev. Sci. Instrum. 66 (3), 2729–2733.
Hanfland, M., Syassen, K., Fahy, S., Louie, S.G., Cohen, M.L., 1986. The 1st-order Raman mode of diamond under pressure. Physica B & C 139 (1–3), 516–519.
Heinz, D.L., 1990. Thermal pressure in the laser-heated diamond anvil cell. Geophys. Res. Lett. 17 (8), 1161–1164.
Hernandez, E.R., Alfe, D., Brodholt, J., 2013. The incorporation of water into lower-mantle perovskites: a first-principles study. Earth Planet. Sci. Lett. 364, 37–43.
Hirschmann, M.M., Withers, A.C., Ardia, P., Foley, N.T., 2012. Solubility of molecular hydrogen in silicate melts and consequences for volatile evolution of terrestrial planets. Earth Planet. Sci. Lett. 345, 38–48.
Ito, E., Katsura, T., 1989. A temperature profile of the mantle transition zone. Geophys. Res. Lett. 16 (5), 425–428.
Kendall, J.M., Silver, P.G., 1996. Constraints from seismic anisotropy on the nature of the lowermost mantle. Nature 381 (6581), 409–412.
Kirby, S.H., Stein, S., Okal, E.A., Rubie, D.C., 1996. Metastable mantle phase transformations and deep earthquakes in subducting oceanic lithosphere. Rev. Geophys. 34 (2), 261–306.
Komabayashi, T., Omori, S., Maruyama, S., 2004. Petrogenetic grid in the system $MgO–SiO_2–H_2O$ up to 30 GPa, 1600 degrees C: applications to hydrous peridotite subducting into the Earth's deep interior. J. Geophys. Res. B 109 (B3).
Komatsu, K., Sano-Furukawa, A., Kagi, H., 2011. Effects of Mg and Si ions on the symmetry of delta-AlOOH. Phys. Chem. Miner. 38 (9), 727–733.
Labrosse, S., Hernlund, J.W., Coltice, N., 2007. A crystallizing dense magma ocean at the base of the Earth's mantle. Nature 450 (7171), 866–869.
Lazor, P., Shen, G., Saxena, S.K., 1993. Laser-heated diamond-anvil cell experiments at high-pressure — melting curve of nickel up to 700 Kbar. Phys. Chem. Miner. 20 (2), 86–90.
Lebail, A., Duroy, H., Fourquet, J.L., 1988. Ab initio structure determination of LiSbWO6 by X-ray-powder diffraction. Mater. Res. Bull. 23 (3), 447–452.
Lesher, C.E., Walker, D., 1988. Cumulate maturation and melt migration in a temperature-gradient. J. Geophys. Res. B 93 (B9), 10295–10311.
Lin, J.F., et al., 2005. Melting behavior of H_2O at high pressures and temperatures. Geophys. Res. Lett. 32 (11).
Litasov, K., et al., 2003. Water solubility in Mg-perovskites, and water storage capacity in the lower mantle. Earth Planet. Sci. Lett. 211 (1–2), 189–203.
Lord, O.T., Walter, M.J., Dasgupta, R., Walker, D., Clark, S.M., 2009. Melting in the Fe–C system to 70 GPa. Earth Planet. Sci. Lett. 284 (1–2), 157–167.
Lord, O.T., et al., 2010. The FeSi phase diagram to 150 GPa. J. Geophys. Res. B 115.
Lord, O.T., et al., 2014. The NiSi melting curve to 70 GPa. Phys. Earth Planet. Inter. 233, 13–23.
Mao, H.K., Xu, J., Bell, P.M., 1986. Calibration of the ruby pressure gauge to 800-Kbar under quasi-hydrostatic conditions. J. Geophys. Res. B 91 (B5), 4673–4676.
Mao, H.K., et al., 1991. Effect of pressure, temperature, and composition on lattice-parameters and density of (Fe, Mg)SiO_3-perovskites to 30 GPa. J. Geophys. Res. B 96 (B5), 8069–8079.
Marty, B., 2012. The origins and concentrations of water, carbon, nitrogen and noble gases on Earth. Earth Planet. Sci. Lett. 313, 56–66.
Meade, C., Reffner, J.A., Ito, E., 1994. Synchrotron infrared absorbency measurements of hydrogen in $MgSiO_3$ perovskite. Science 264 (5165), 1558–1560.
Mookherjee, M., Stixrude, L., Karki, B., 2008. Hydrous silicate melt at high pressure. Nature 452 (7190), 983–986.
Mosenfelder, J.L., Asimow, P.D., Ahrens, T.J., 2007. Thermodynamic properties of Mg_2SiO_4 liquid at ultra-high pressures from shock measurements to 200 GPa on forsterite and wadsleyite. J. Geophys. Res. B 112 (B6).
Mukhopadhyay, S., 2012. Early differentiation and volatile accretion recorded in deep-mantle neon and xenon. Nature 486 (7401) (101-U124).
Murakami, M., Hirose, K., Yurimoto, H., Nakashima, S., Takafuji, N., 2002. Water in Earth's lower mantle. Science 295 (5561), 1885–1887.
Murakami, M., Hirose, K., Kawamura, K., Sata, N., Ohishi, Y., 2004. Post-perovskite phase transition in $MgSiO_3$. Science 304 (5672), 855–858.
Mysen, B.O., Fogel, M.L., Morrill, P.L., Cody, G.D., 2009. Solution behavior of reduced C-O-H volatiles in silicate melts at high pressure and temperature. Geochim. Cosmochim. Acta 73 (6), 1696–1710.
Navrotsky, A., 1999. Mantle geochemistry — a lesson from ceramics. Science 284 (5421), 1788–1789.
Navrotsky, A., et al., 2003. Aluminum in magnesium silicate perovskite: formation, structure, and energetics of magnesium-rich defect solid solutions. J. Geophys. Res. B 108 (B7).
Nishi, M., et al., 2014. Stability of hydrous silicate at high pressures and water transport to the deep lower mantle. Nat. Geosci. 7 (3), 224–227.
Nowacki, A., Wookey, J., Kendall, J.M., 2010. Deformation of the lowermost mantle from seismic anisotropy. Nature 467 (7319), 1091–1095.
Nowacki, A., Walker, A.M., Wookey, J., Kendall, J.M., 2013. Evaluating post-perovskite as a cause of D″ anisotropy in regions of palaeosubduction. Geophys. J. Int. 192 (3), 1085–1090.
Ohira, I., et al., 2014. Stability of a hydrous delta-phase, AlOOH-$MgSiO_2(OH)_2$, and a mechanism for water transport into the base of lower mantle. Earth Planet. Sci. Lett. 401, 12–17.
Ohtani, E., 2005. Water in the mantle. Elements 1 (1), 25–30.
Ohtani, E., Mizobata, H., Yurimoto, H., 2000. Stability of dense hydrous magnesium silicate phases in the systems $Mg_2SiO_4–H_2O$ and $MgSiO_3–H_2O$ at pressures up to 27 GPa. Phys. Chem. Miner. 27 (8), 533–544.
Ohtani, E., Litasov, K., Suzuki, A., Kondo, T., 2001a. Stability field of new hydrous phase, delta-AlOOH, with implications for water transport into the deep mantle. Geophys. Res. Lett. 28 (20), 3991–3993.
Ohtani, E., Toma, M., Litasov, K., Kubo, T., Suzuki, A., 2001b. Stability of dense hydrous magnesium silicate phases and water storage capacity in the transition zone and lower mantle. Phys. Earth Planet. Inter. 124 (1–2), 105–117.
Ohtani, E., Litasov, K., Hosoya, T., Kubo, T., Kondo, T., 2004. Water transport into the deep mantle and formation of a hydrous transition zone. Phys. Earth Planet. Inter. 143, 255–269.
Ono, S., Oganov, A.R., 2005. In situ observations of phase transition between perovskite and $CaIrO_3$-type phase in $MgSiO_3$ and pyrolitic mantle composition. Earth Planet. Sci. Lett. 236 (3–4), 914–932.
Pamato, M.G., et al., 2015. Lower-mantle water reservoir implied by the extreme stability of a hydrous aluminosilicate. Nat. Geosci. 8 (1), 75–79.

Sano, A., et al., 2008. Aluminous hydrous mineral delta-AlOOH as a carrier of hydrogen into the core–mantle boundary. Geophys. Res. Lett. 35 (3).
Schmandt, B., Jacobsen, S.D., Becker, T.W., Liu, Z., Dueker, K.G., 2014. Earth's interior dehydration melting at the top of the lower mantle. Science 344 (6189), 1265–1268.
Schwager, B., Boehler, R., 2008. H(2)O: another ice phase and its melting curve. High Pressure Res. 28 (3), 431–433.
Schwager, B., Chudinovskikh, L., Gavriliuk, A., Boehler, R., 2004. Melting curve of H_2O to 90 GPa measured in a laser-heated diamond cell. J. Phys. Condens. Matter 16 (14), S1177–S1179.
Schwegler, E., Sharma, M., Gygi, F., Galli, G., 2008. Melting of ice under pressure. Proc. Natl. Acad. Sci. U. S. A. 105 (39), 14779–14783.
Shen, G.Y., Lazor, P., 1995. Measurement of melting temperatures of some minerals under lower mantle pressures. J. Geophys. Res. B 100 (B9), 17699–17713.
Shieh, S.R., Mao, H.K., Hemley, R.J., Ming, L.C., 1998. Decomposition of phase D in the lower mantle and the fate of dense hydrous silicates in subducting slabs. Earth Planet. Sci. Lett. 159 (1–2), 13–23.
Shinmei, T., Irifune, T., Tsuchiya, J., Funakoshi, K.-I., 2008. Phase transition and compression behavior of phase D up to 46 GPa using multi-anvil apparatus with sintered diamond anvils. High Pressure Res. 28 (3), 363–373.
Sinmyo, R., Hirose, K., 2010. The Soret diffusion in laser-heated diamond-anvil cell. Phys. Earth Planet. Inter. 180 (3–4), 172–178.
Spektor, K., et al., 2011. Ultrahydrous stishovite from high-pressure hydrothermal treatment of SiO_2. Proc. Natl. Acad. Sci. U. S. A. 108 (52), 20918–20922.
Stixrude, L., Karki, B., 2005. Structure and freezing of $MgSiO_3$ liquid in Earth's lower mantle. Science 310 (5746), 297–299.
Suzuki, A., Ohtani, E., Kamada, T., 2000. A new hydrous phase delta-AlOOH synthesized at 21 GPa and 1000 degrees C. Phys. Chem. Miner. 27 (10), 689–693.
Syracuse, E.M., van Keken, P.E., Abers, G.A., 2010. The global range of subduction zone thermal models. Phys. Earth Planet. Inter. 183 (1–2), 73–90.
Tateno, S., Hirose, K., Sata, N., Ohishi, Y., 2005. Phase relations in $Mg_3Al_2Si_3O_{12}$ to 180 GPa: effect of Al on post-perovskite phase transition. Geophys. Res. Lett. 32 (15).
Thomson, A., Walter, M.J., Lord, O.T., Kohn, S.C., 2014. Experimental determination of the eutectic melting curves in the systems enstatite–magnesite and magnesite–calcite from 15–80 GPa. Am. Mineral. 99, 1544–1554.
Toby, B.H., 2001. EXPGUI, a graphical user interface for GSAS. J. Appl. Crystallogr. 34, 210–213.
Tsuchiya, J., 2013. First principles prediction of a new high-pressure phase of dense hydrous magnesium silicates in the lower mantle. Geophys. Res. Lett. 40 (17), 4570–4573.
Tsuchiya, J., Tsuchiya, T., Tsuneyuki, S., Yamanaka, T., 2002. First principles calculation of a high-pressure hydrous phase, delta-AlOOH. Geophys. Res. Lett. 29 (19).
Walter, M.J., Koga, K.T., 2004. The effects of chromatic dispersion on temperature measurement in the laser-heated diamond anvil cell. Phys. Earth Planet. Inter. 143, 541–558.
Walter, M.J., et al., 2004. Phase relations and equation-of-state of aluminous Mg-silicate perovskite and implications for Earth's lower mantle. Earth Planet. Sci. Lett. 222 (2), 501–516.
Walter, M.J., et al., 2006. Subsolidus phase relations and perovskite compressibility in the system MgO–AlO1.5–SiO_2 with implications for Earth's lower mantle. Earth Planet. Sci. Lett. 248 (1–2), 77–89.